

1 **Computation-guided optimization of split protein systems**

2

3 Taylor B. Dolberg<sup>1,2,9</sup>, Anthony T. Meger<sup>3,4,9</sup>, Jonathan D. Boucher<sup>2,5</sup>, William K. Corcoran<sup>2,5</sup>, Elizabeth E.

4 Schauer<sup>1,2</sup>, Alexis N. Prybutok<sup>1,2</sup>, Srivatsan Raman<sup>3,4,8\*</sup>, Joshua N. Leonard<sup>1,2,5,6,7\*</sup>

5

6

7 <sup>1</sup>Department of Chemical and Biological Engineering, Northwestern University, Evanston, Illinois 60208,

8 United States

9 <sup>2</sup>Center for Synthetic Biology, Northwestern University, Evanston, Illinois 60208, United States

10 <sup>3</sup>Department of Biochemistry, University of Wisconsin-Madison, Madison, Wisconsin 53706, United States

11 <sup>4</sup>Great Lakes Bioenergy Research Center, University of Wisconsin-Madison, Madison, Wisconsin 53706,

12 United States

13 <sup>5</sup>Interdisciplinary Biological Sciences Program, Northwestern University, Evanston, Illinois 60208, United

14 States

15 <sup>6</sup>Chemistry of Life Processes Institute, Northwestern University, Evanston, Illinois 60208, United States

16 <sup>7</sup>Member, Robert H. Lurie Comprehensive Cancer Center, Northwestern University, Evanston, Illinois

17 60208, United States

18 <sup>8</sup>Department of Bacteriology, University of Wisconsin-Madison, Madison, Wisconsin 53706, United States

19 <sup>9</sup>These authors contributed equally to this work

20

21 **Contact Information**

22 \*Corresponding authors: Srivatsan Raman ([sraman4@wisc.edu](mailto:sraman4@wisc.edu)) and Joshua N. Leonard ([23 \[leonard@northwestern.edu\]\(mailto:leonard@northwestern.edu\)\)](mailto:j-</a></p></div><div data-bbox=)

24

25 **ABSTRACT**

26 Splitting bioactive proteins, such as enzymes or fluorescent reporters, into conditionally reconstituting  
27 fragments is a powerful strategy for building tools to study and control biochemical systems. However, split  
28 proteins often exhibit a high propensity to reconstitute even in the absence of the conditional trigger, which  
29 limits their utility. Current approaches for tuning reconstitution propensity are laborious, context-specific, or  
30 often ineffective. Here, we report a computational design-driven strategy that is grounded in fundamental  
31 protein biophysics and which guides the experimental evaluation of a focused, sparse set of mutants—  
32 which vary in the degree of interfacial destabilization while preserving features such as stability and catalytic  
33 activity—to identify an optimal functional window. We validate our method by solving two distinct split  
34 protein design challenges, generating both broad insights and new technology platforms. This method will  
35 streamline the generation and use of split protein systems for diverse applications.

36

37 **KEYWORDS:** synthetic biology, split proteins, computational protein design, protein engineering

38

## 39 INTRODUCTION

40

41 Split proteins and conditional reconstitution systems are powerful tools for interrogating biology and  
42 controlling cell behavior.<sup>1-4</sup> These systems work by splitting a protein into two fragments to disrupt the  
43 protein's function. Each fragment is then fused to a partner domain such that the split protein is  
44 reconstituted, and its function is restored only when the partner domains interact. This modular strategy  
45 may be applied to diverse functional proteins to control bioluminescence<sup>5, 6</sup>, fluorescence<sup>7</sup>, proteolytic  
46 cleavage<sup>8-10</sup> and transcription<sup>11, 12</sup>. As a result, conditionally-reconstituted split proteins have been  
47 employed in a variety of applications including probing and discovering new protein-protein interactions<sup>13-</sup>  
48 <sup>16</sup>, studying post-translational modifications<sup>17</sup>, imposing small molecule-regulated control over enzymatic  
49 activity<sup>18, 19</sup>, and rewiring cellular signaling<sup>9, 20</sup>.

50

51 Despite their utility in certain contexts, broader application of split protein systems is largely limited by the  
52 spontaneous reconstitution of fragments, resulting in high background activity (**Fig. 1a**). Splitting a protein  
53 tends to expose its hydrophobic core, creating highly unfavorable interactions between the core and  
54 solvent. Reconstitution is driven by a strong inherent preference to desolvate by recombining the fragments.  
55 Evaluating alternative splitting sites can vary reconstitution propensity, but this approach often only partially  
56 ameliorates the problem because changing splitting sites may not significantly affect underlying  
57 hydrophobic forces. Therefore, it is necessary to identify variants with a reconstitution propensity that  
58 precludes spontaneous reconstitution but enables reconstitution under desired conditions. Variants with a  
59 range of reconstitution propensities can be generated by random mutagenesis and screened for the desired  
60 property. However, high-throughput screening is not readily available for all split protein systems, and low-  
61 throughput clonal testing of variants can be laborious and suffer from inefficient exploration of sequence  
62 space. Even when screens generate improved variants, it may be difficult to interpret why only certain  
63 mutants were successful, and as a result, generalizable rules cannot be transferred to guide the tuning of  
64 new split protein systems. Furthermore, split protein systems tuned by mutagenesis exhibit performance  
65 characteristics determined by (and limited to) the conditions used in the initial screens, again posing a  
66 barrier to general applications.

67  
68 Here, we report a general strategy based on fundamental principles of protein biophysics for optimizing  
69 split protein systems which we term **S**plit **P**rotein **O**ptimization by **R**econstitution **T**uning, or SPORT. We  
70 use computational mutagenesis with the Rosetta macromolecular modeling suite to guide limited  
71 experimental screening and thereby discretely map the sequence-energy landscape of the split interface.  
72 This allows us to determine optimal interaction energies that maximize the performance of the split protein  
73 system. We demonstrate proof-of-concept by optimizing a split protease system for conditional  
74 reconstitution in two different contexts: membrane-embedded and cytosolic. Our approach generates  
75 simple design rules that may be extended to tune other split protein systems for distinct design goals and  
76 can be implemented by most research laboratories. This work demonstrates a new method for efficiently  
77 engineering split protein systems, which will streamline the generation and expand the use of split protein  
78 systems for diverse applications.

## 79 80 **RESULTS**

### 81 82 **Formulation of the design challenge and strategy**

83  
84 As a first step toward developing a strategy that addresses the challenge of designing split proteins, we  
85 selected a model system based on the well-studied Tobacco Etch Virus protease (TEVp)—we sought to  
86 tune the reconstitution propensity of split TEVp. For this purpose, we modified a synthetic receptor system  
87 that we previously reported (Modular Extracellular Split Architecture, or MESA)<sup>21</sup> to serve as a reporter of  
88 conditional split TEVp reconstitution. In this testbed, ligand binding-induced dimerization of a membrane  
89 receptor reconstitutes an intracellular split TEVp, which then autolytically liberates a sequestered  
90 transcription factor to drive reporter gene expression (**Fig. 1b**). Our initial evaluation demonstrated that the  
91 canonical split TEVp (split between residues 118/119)<sup>22</sup> showed high propensity to reconstitute, resulting  
92 in high background from ligand-independent signaling (**Supplementary Fig. 1**). As the original screens  
93 used to identify this split were performed in a soluble rather than membrane-bound context, these data  
94 suggest that tethering split TEVp to a membrane may promote reconstitution. Furthermore, we determined

95 that this problem is not limited to the canonical split site, as other TEVp partitioning also yielded poor  
96 performance (**Supplementary Fig. 2**). Given these observations, we formulated a design goal: rationally  
97 mutate split TEVp to optimize two key MESA performance characteristics—minimal reporter gene  
98 expression in the absence of ligand and a substantial fold increase in reporter expression upon ligand  
99 addition.

100

## 101 **Biophysical principles underlying SPORT**

102

103 We developed SPORT, a computation-guided workflow to rationally design split protein interfaces to  
104 optimize reconstitution propensity (**Fig. 1c**). SPORT employs Rosetta, a state-of-the-art software package  
105 for protein design.<sup>23</sup> Given a protein with a predetermined split site, our first step was to identify key  
106 interfacial residues to target for mutagenesis. Residues with large differences in solvent-accessible surface  
107 area (SASA)—when comparing intact protein and split fragments—were classified as buried residues.  
108 These buried residues are ideal targets for mutagenesis as they likely contribute substantially to the driving  
109 force for spontaneous reconstitution. For each buried residue, we performed a comprehensive, *in silico*  
110 mutational scan to evaluate the energy perturbation of all possible single-point mutations on the interaction  
111 energy across the split protein interface ( $\Delta\Delta G_{\text{Interfacial}}$ ) and total stability of the mutated protein ( $\Delta\Delta G_{\text{Total}}$ )  
112 relative to the parent. The degree of disruption is a critical design consideration. Insufficient disruption may  
113 retain high background activity while excessive disruption may impair catalytic activity due to loss of overall  
114 protein stability. Therefore, the interface must be carefully tuned so that the driving force provided by ligand  
115 binding-induced dimerization promotes reconstitution. This “Goldilocks zone” likely differs for each  
116 individual protein and perhaps depends upon context, and this zone is difficult to define *a priori*. Therefore,  
117 our strategy was to identify the Goldilocks zone for a given protein by choosing mutations that span the  
118 range of  $\Delta\Delta G$  values. We hypothesized that a limited test set of mutants would direct subsequent  
119 mutagenesis efforts by predicting desirable mutant combinations from a vast amount of sequence space.  
120 Each of these propositions was tested using experimental case studies.

121

## 122 **Validating SPORT by tuning a membrane-tethered split TEV protease**

123  
124 To investigate and validate SPORT, we applied our design workflow to the split TEVp MESA system. We  
125 first assessed the per-residue change in solvent accessible surface area ( $\Delta$ SASA) between the intact form  
126 and split fragments (**Fig. 2a**). In total, 130 of the 218 residues showed increased SASA in the isolated  
127 fragments. We excluded from this set the catalytic triad and 27 residues lying within a 6 Å coordination  
128 sphere around the catalytic triad to avoid perturbing the catalytic function of reconstituted TEVp. Of the  
129 remaining 100 positions, we chose the 15 positions with the largest  $\Delta$ SASA (9 in N-terminal and 6 in C-  
130 terminal halves of split TEVp) as candidates for mutagenesis. Next, we evaluated the energy perturbation  
131 of all possible single-point mutations (285 in total) at these positions using Rosetta. As expected, few  
132 mutations were predicted to increase stability, and a vast majority were destabilizing (**Fig. 2b**,  
133 **Supplementary Figure 3**). Many positions exhibited a variety of stabilizing, benign, and destabilizing point  
134 mutations that were consistent with structure. For instance, bulky sidechain substitutions (W, F, Y, R, K and  
135 H) at position 103 resulted in many steric clashes with neighboring residues (**Fig. 2b** right panel) and  
136 subsequently conferred large decreases in predicted stability.

137  
138 Guided by these predictions, we next experimentally characterized 20 single-mutant split TEV variants that  
139 span a wide range of  $\Delta\Delta G_{\text{Interfacial}}$  (3.1 to 16.1 Rosetta Energy Units, or REU) and  $\Delta\Delta G_{\text{Total}}$  (-1.9 to 30 REU)  
140 energies (**Fig. 2c**). We observed high background signaling (i.e., reporter expression) for disruptions up to  
141  $\Delta\Delta G_{\text{Interfacial}} \sim 6.6$  REU, which suggested that destabilization was insufficient. However, four out of ten  
142 variants with  $\Delta\Delta G_{\text{Interfacial}} > 10$  REU exhibited reduced background signaling and substantial ligand-induced  
143 activation (**Fig. 2c**). The remaining six were completely inactive (or “dead”); they induced no signaling under  
144 any conditions. Energy-based partitioning across different phenotypes (inducible, not inducible, and dead)  
145 became evident when comparing  $\Delta\Delta G_{\text{Interfacial}}$  and  $\Delta\Delta G_{\text{Total}}$  of all 20 single mutant split TEV variants (**Fig.**  
146 **2d**). Variants with high background activity due to insufficient destabilization fell in the region where  
147  $\Delta\Delta G_{\text{Interfacial}} < 10$  and  $\Delta\Delta G_{\text{Total}} < 10$  REU. Variants with the dead phenotype had  $\Delta\Delta G_{\text{Interfacial}} > 10$  and  
148  $\Delta\Delta G_{\text{Total}} > 10$  REU; since these mutants were expressed, as confirmed by Western blot (**Supplementary**  
149 **Fig. 4**), the lack of signaling suggested that these mutations directly preclude reconstitution. Most of the  
150 inducible variants (three out of four) were observed in the energy window where  $\Delta\Delta G_{\text{Interfacial}} > 10$  and

151  $\Delta\Delta G_{\text{Total}} < 10$  REU, which may represent the Goldilocks zone we hypothesized to exist. An additional region  
152 contained a mixture of inducible and dead phenotypes. By inspection of these results, we then proposed a  
153 model for broadly classifying experimental phenotypes based on energy partitions (**Fig. 2e**).

154

### 155 **SPORT predicts outcomes of combining mutations**

156

157 We next evaluated whether our proposed classifier model—developed based upon observations with single  
158 mutants—could predict the phenotypes of combined NTEVp and CTEVp mutations, including both double  
159 (two mutations on one chain) and paired (one mutation on each chain) mutants derived by combining the  
160 initial 14 single non-dead mutations tested (**Fig. 3a**). Of the 67 possible double and paired mutants tested,  
161 28 were predicted to be inducible. We experimentally tested 14 of these and found that 10 exhibited  
162 inducible signaling as predicted, one was dead, and three were not inducible; this yields an observed  
163 accuracy of 0.71 for inducible predictions (**Fig. 3b,c**). Interestingly, three of the prediction failures fell at the  
164 low end of the range of predicted changes in interfacial energy, suggesting potential opportunities for  
165 refining the classifier model. We also noted an interesting trend in our  $\Delta\Delta G$  (total and interfacial)  
166 calculations—for the sixty-seven mutants tested, the calculated  $\Delta\Delta G$  for the double and paired mutants  
167 were nearly identical to the sums of the  $\Delta\Delta G$  calculated for the associated single mutants (**Supplementary**  
168 **Fig. 5**). Thus, for subsequent analyses of combined mutants, we simply added the effects of single mutants  
169 in our calculations.

170

171 We next investigated how variations in expression level might impact the inducibility of the mutants. We  
172 used Western blot analysis to normalize and vary chain expression levels by adjusting DNA doses  
173 (**Supplementary Fig. 6**). Notably, these constructs remained inducible across the entire range of  
174 expression levels tested, suggesting that the biophysical mechanism of optimized split protein reconstitution  
175 is robust to variations in the expression levels and ratio of the membrane-bound split TEVp fragments.  
176 However, we observed that the performance of these constructs (i.e., fold induction of signaling upon ligand  
177 addition) could be substantially improved through tuning expression such that protein levels of each  
178 fragment are comparable (**Fig. 3d, Supplementary Fig. 7**). Taken together, these results suggest that a

179 classifier calibrated with a limited set of experimental observations spanning the full range of  $\Delta\Delta G$  can  
180 predict function of new mutants with high accuracy in a manner that is independent of expression level of  
181 the construct.

182

### 183 **SPORT predicts phenotypes of novel mutations and combinations**

184

185 All mutations previously tested were derived from predictions based on our computational method. Next,  
186 we wanted to test a broad set of mutants (outside the calibration set) to investigate the accuracy of our  
187 classification scheme. Therefore, we experimentally characterized additional single mutants (not included  
188 in the original calibration set) and all combinations of paired mutations derived from both the original and  
189 this expanded mutation set (omitting dead constructs); mutants were selected to explore the boundaries of  
190 the energy landscape classifier model and were expected to reflect a wide range of induced and uninduced  
191 reporter expression levels and ratios (**Figs. 2e, 3a**). We also sought to investigate whether the phenotypic  
192 partitioning demonstrated for inducibility (**Fig. 3b,c**) is extensible to the other phenotype classes (i.e., dead  
193 and not inducible). This expanded set paired 10 N-terminal mutations with 16 C-terminal mutations. In  
194 general, we observed that variants with larger  $\Delta\Delta G_{\text{interfacial}}$  energies had lower reporter expression levels in  
195 both the background (OFF) and ligand-induced (ON) states (**Fig. 4a**, left and middle panels). Thus, the cost  
196 of lowering the OFF state is to also lower the ON state, but these reductions are not always proportional.  
197 This is evident by the diversity of calculated fold inductions (**Fig. 4a**, right panel). Only one variant,  
198 H75P/W198E, exhibited a significant decrease in the OFF state and an increase in the ON state relative to  
199 wild type (WT). However, the variants with highest fold inductions, such as H75S/I163P (17.3 fold induction)  
200 and H75T/I163P (9.92 fold induction), exhibited significantly lower OFF and ON states than did the WT,  
201 reflecting a tradeoff between desirable performance characteristics. Overall, we observed moderate  
202 agreement between the actual and predicted phenotypes for these novel variants and combinations (**Fig.**  
203 **4b**). The classifier model was most accurate for predicting the not inducible phenotype (25 of 29, 86%).  
204 Many inducible phenotype predictions were also confirmed (31 of 52, 60%). This success rate is impressive  
205 given that phenotypic classification boundaries were set roughly based upon the sparse calibration set (**Fig.**



206 **2e)**. Interestingly, this analysis also indicates that the energy landscape calculated by SPORT correlates  
207 with each phenotype to differing degrees.

208

209 In order to gain additional insight into how choice of calibration set and sample size may impact the accuracy  
210 of SPORT predictions, we performed retrospective bootstrapping analysis of the data presented in **Figure**  
211 **4** (see **Supplementary Note 2** for full details). Experimental data were stratified by the energy landscape  
212 and partitioned randomly into calibration and prediction subsets. Logistic regression modeling was applied  
213 to evaluate the accuracy of classification under various conditions (**Supplementary Fig. 8**). We observed  
214 robust prediction accuracy using multiple unique calibration sets and using sample sizes ranging from 4 to  
215 28. This outcome suggests that our ability to generate a general classification model was not dependent  
216 upon the specific calibration data we used in our initial characterization experiment (**Fig. 2**), and that a  
217 relatively small set of calibration data drawn from a distribution like that included in **Figure 4** would be  
218 sufficient to generate a general classification model.

219

## 220 **Extension of SPORT predictions to new design goals**

221

222 A major limitation to current approaches for employing split proteins is that often a variant selected to  
223 perform well in one context fails in a different context. To investigate whether the SPORT design method is  
224 generalizable beyond our initial model system, we developed a distinct model system. This new system  
225 employs split TEVp in a soluble form, where we hypothesized that a different reconstitution propensity  
226 would be required compared to the membrane-bound model system. To generate such a soluble test  
227 system (**Fig. 5a**), ligand binding domains were fused to split TEVp domains along with a soluble  
228 transcription factor flanked by protease cleavage sites and nuclear export signals (NES); thus, TEVp-  
229 mediated cleavage removes the NES from the transcription factor to enable nuclear localization and  
230 reporter expression. We first developed and tested a panel of soluble transcription factors that could  
231 implement this mechanism. This evaluation included varying the number of NES elements, their placement  
232 at N and/or C terminus of the transcription factor, and the P1' residue of the TEVp cleavage sequence  
233 which governs cleavage kinetics<sup>24</sup> (**Fig. 5b**). Several soluble transcription factor constructs exhibited the

234 desired phenotype of low signaling in the absence of TEVp and high signaling when co-expressed with full  
235 TEVp; construct TF10 was selected for evaluating split TEVp variants.

236

237 Using our soluble split TEVp test system, we evaluated a panel of 10 single TEVp mutants and 10 paired  
238 TEVp mutants spanning a range of interfacial energies (**Fig. 5c**). The construct based upon WT split TEVp  
239 exhibited a substantial fold induction, which is consistent with the fact that this split protein was identified  
240 by screens performed in the soluble phase<sup>22</sup>. However, the WT construct also yielded high background  
241 signaling in the absence of ligand, indicating an opportunity to improve performance. For modest increases  
242 in  $\Delta\Delta G_{\text{Interfacial}}$  (~0–3.6 REU), background signaling persisted. For intermediate increases in  $\Delta\Delta G_{\text{Interfacial}}$  (~6–  
243 10 REU), a mixture of phenotypes was observed, including dead constructs and those with both  
244 substantially reduced background signaling and substantial fold inductions. For large increase in  
245  $\Delta\Delta G_{\text{Interfacial}} > \sim 10$  REU, constructs were generally weakly-inducible or dead. Thus, a focused evaluation of  
246 20 design variants, guided by SPORT, yielded ~5 variants exhibiting improved performance compared to  
247 the WT construct. Altogether, these observations demonstrate that the SPORT method and associated  
248 energy landscape concept can be employed to efficiently solve distinct split protein optimization challenges.

249

## 250 **DISCUSSION**

251

252 In this study, we developed and validated what is—to our knowledge—the first computational strategy for  
253 tuning split protein reconstitution propensity. Although the split TEVp MESA used as our first model system  
254 would have been deemed infeasible using standard evaluations of split proteins (**Supplementary Figs. 1-**  
255 **2**), application of SPORT to tune this system yielded multiple high-performing new synthetic receptor  
256 scaffolds (**Fig. 3d**). We show that unlike the classical MESA receptors we have characterized in prior work<sup>21</sup>,  
257 <sup>25, 26</sup>, split TEVp MESA tuned by SPORT exhibit excellent performance characteristics (i.e., low-background  
258 and high fold-induction) in a manner that is robust to variations in both biosensor expression level and the  
259 ratio at which biosensor chains are expressed (**Supplementary Figure 7**). This property is of great practical  
260 utility, as it precludes the need to carefully tune the implementation of each biosensor.

261

262 Several important insights emerged from this study. First, our approach demonstrated that testing a sparse  
263 set of mutants along the energy landscape is an effective strategy to choose optimal interfacial energies to  
264 promote conditional reconstitution. Second, multiple point mutations with similar energies exhibited similar  
265 performance, which suggests reconstitution propensity depends on the energy of destabilization but is  
266 agnostic to specific mutations. Third, the concept of a Goldilocks zone is likely generalizable to different  
267 proteins and application contexts, but the optimal energy window may have to be adjusted on a case-by-  
268 case basis. We find that membrane-bound split proteins must be destabilized to a greater degree than  
269 soluble split proteins in order to avoid spontaneous reconstitution. Altogether, these results show that split  
270 protein systems can be engineered based on fundamental principles of protein biophysics, which obviates  
271 the need for exhaustive screening and generates rules applicable to new candidate proteins.

272  
273 There are several interesting opportunities for extending and improving SPORT in future work. First,  
274 although our analysis showed that SPORT can be used to identify mutations that confer specific energy  
275 changes, it does not yet enable *a priori* prediction of where the Goldilocks zone will fall for new applications.  
276 It is possible that subsequent analysis of many case studies could identify trends that enable such  
277 predictions and thus harness SPORT to further focus experimental investigations. An additional opportunity  
278 is pairing SPORT with a multiparametric optimization framework for exploring pareto-optimal tradeoffs  
279 between performance characteristics; for example, in our model system, there seems to be such a tradeoff  
280 between low background in the ligand-free state and high signaling in the ligand-induced state. Finally, the  
281 SPORT algorithm itself may be refined to better avoid false positives (e.g., dead mutants that share a region  
282 of the energy landscape with inducible variants). Altogether, our findings suggest many opportunities for  
283 expanding the utility of split proteins for many new applications and highlight the impact of SPORT-guided  
284 development of novel biochemical and synthetic biology tools.

285

286

## 287 **METHODS**

288

### 289 **General DNA assembly**

290 Plasmid cloning was performed using standard molecular biology techniques of PCR and restriction  
291 enzyme cloning with Phusion DNA Polymerase (NEB), restriction enzymes (NEB; Thermo Fisher), T4 DNA  
292 Ligase (NEB), and Antarctic Phosphatase (NEB). Development of the tTA-responsive YFP reporter plasmid  
293 was described previously<sup>21</sup>. Plasmids were transformed into chemically competent TOP10 *E. coli* (Thermo  
294 Fisher) and grown at 37°C. Plasmid maps are provided as GenBank files (**Supplementary Data 1**).

295

### 296 **Plasmid preparation**

297 Plasmid DNA used for transfection was prepared using the PEG precipitation method, which was previously  
298 described in detail.<sup>27</sup>

299

### 300 **Cell culture**

301 HEK293FT cells (Life Technologies/Thermo) were maintained at 37°C incubator and 5% CO<sub>2</sub>. Cells were  
302 cultured in DMEM (Gibco 31600-091) with 10% FBS, 6 mM L-glutamine (2 mM from Gibco 31600-091 and  
303 4 mM from additional Gibco 25030-081), penicillin (100 U/μL), and streptomycin (100 μg/mL) (Gibco  
304 15140122).

305

### 306 **Transfection**

307 Transfections were performed in 24 well plates seeded at 1.5 x 10<sup>5</sup> cell in 0.5 mL of DMEM media. At 6-8  
308 hours post-seeding, cells were transfected using calcium phosphate method with a total DNA content of 1-  
309 2 ug DNA per mL of media, using DNA prepared by PEG precipitation. All experiments included blue  
310 fluorescent protein (BFP) as a control to assess transfection efficiency. The exact DNA amounts added to  
311 the mix per well are as follows, unless otherwise stated in figure captions: 25 ng of each TEVp chain, 200  
312 ng of BFP control, 200 ng of YFP reporter plasmid, and 150 ng of pcDNA plasmid. This mixture was added  
313 dropwise to an equal-volume solution of 2x HEPES-Buffered Saline (280 mM NaCl, 0.5 M HEPES, 1.5 mM  
314 Na<sub>2</sub>HPO<sub>4</sub>) and gently pipetted up and down four times. After 2.5 minutes, the solution was mixed vigorously  
315 by pipetting ten times and 100 μL of this mixture was added dropwise to each well of the plated cells, and  
316 the plates were swirled gently. For functional experiments, 12 hours post-transfection, media containing 0.1  
317 μM rapamycin analog (Takara AP21967) or 0.1% ethanol as a control was added to cells. At 24-30 hours

318 post-media change, cells were harvested for flow cytometry with Trypsin-EDTA, which was then quenched  
319 with medium, and the resulting cell solution was added to at least 2 volumes of FACS buffer (PBS pH 7.4  
320 with 2–5 mM EDTA and 0.1% BSA). Cells were spun at 150 x g for 5 min, FACS buffer was decanted, and  
321 fresh FACS buffer was added. All experiments were performed in biological triplicate.

322

### 323 **Flow Cytometry**

324 Approximately  $10^4$  live cells from each transfected well of the 24-well plate were analyzed using a BD LSR  
325 Fortessa Special Order Research Product (Robert H. Lurie Cancer Center Flow Cytometry Core) running  
326 FACSDiva software. Samples were analyzed using FlowJo v10 software (FlowJo, LLC). The HEK293FT  
327 cell population was identified by FSC-A vs. SSC-A gating, and singlets were identified by FSC-A vs. FSC-  
328 H gating. A control sample of cells—generated by transfecting cells with a mass of pcDNA (empty vector)  
329 equivalent to the mass of DNA used in other samples in the experiment—was used to distinguish  
330 transfected and non-transfected cells. For the single-cell subpopulation of the pcDNA-only sample, a gate  
331 was made to identify cells that were positive for the constitutively driven blue fluorescent protein (BFP) used  
332 as a transfection control in other samples such that the gate included no more than 1% of the non-  
333 fluorescent cells. The mean fluorescence intensity (MFI) of the single-cell transfected population was  
334 calculated and exported for further analysis. BD LSR Fortessa settings used were as follows: BFP was  
335 collected in the Pacific Blue channel (405 nm excitation, 450/50 nm filter) and EYFP was collected in the  
336 FITC channel (488 nm excitation, 505 LP and 530/30 nm filter). To quantify reporter expression, the FITC  
337 channel MFI was averaged across three biological replicates. Cell autofluorescence was subtracted and  
338 MFI was converted to Mean Equivalents of Fluorescein (MEFLs) using the coefficient determined by the  
339 calibration curve of UltraRainbow Calibration Particles (Spherotech URCP-100-2H) run in each individual  
340 experiment. Standard error was propagated through all calculations.

341

### 342 **Western Blotting**

343 Western blots were performed to evaluate protein expression and normalize total expression of each TEVp  
344 chain. A 3X-FLAG tagged NanoLuciferase as a normalization control, and images were analyzed using  
345 ImageJ software. A detailed western blot protocol was previously described.<sup>27</sup>

346

### 347 **Solvent-accessible Surface Area**

348 The structure of TEVp was obtained from the Research Crystallography for Structural Bioinformatics  
349 (RCSB) PDB (ID code: 1LVM). Per-residue solvent-accessible surface areas (SASA) were computed using  
350 GROMACS v2018.1, which utilizes the double cubic lattice method (DCLM) described by Eisenhaber et  
351 al.<sup>28</sup> The change in solvent accessible area was computed as

$$352 \quad \Delta SASA = SASA_{fragments} - SASA_{reconstituted}$$

353 where structures of the N and C-terminal fragments were isolated from the crystal structure.

354

### 355 **Computational Interface Scanning**

356 All modeling calculations were performed using the *Rosetta* molecular modeling suite v3.9. Single-point  
357 mutants were generated using the standard Relax application, which enables local conformational sampling  
358 to minimize energy (**Supplementary Note 1** includes full details). The total energy ( $\Delta G_{Total}$ ) of each mutant  
359 was computed as the average of 100 relaxed models. The energy perturbation to total energy was  
360 computed as

$$361 \quad \Delta \Delta G_{Total} = \Delta G_{Total}^{Mutant} - \Delta G_{Total}^{WT}$$

362 The Rosetta Scripts application with the InterfaceAnalyzeMover was applied to each relaxed model to  
363 compute the average residue-residue interaction energies between the N- and C-terminal fragments  
364 (**Supplementary Note 1** includes the full details). The interfacial energy was computed as the pair-wise  
365 sum of all short-range interaction energies as shown by

$$366 \quad \Delta G_{Interfacial} = \sum_i \sum_j Energy_{i-j}^{SR}$$

367 where *i* and *j* denote the sets of residues within each fragment. The energy perturbation of each mutation  
368 to the interfacial energy was then computed as

$$369 \quad \Delta \Delta G_{Interfacial} = \Delta G_{Interfacial}^{Mutant} - \Delta G_{Interfacial}^{WT}$$

370

### 371 **Phenotype Classifier**

372 Experimentally characterized variants were assigned class labels (not-inducible, inducible and dead) based  
373 on reporter expression levels in the ligand-absent and ligand-induced states. Variants with  $\geq 1.2$  fold higher  
374 reporter expression in the ligand-induced state relative to the ligand-absent state were labeled as inducible.  
375 For variants with expression levels  $< 5\%$  of wild-type (WT) sequence in the ligand-induced state and  $< 1.2$   
376 fold activation were classified as functionally dead. The remaining variants were assigned the not-inducible  
377 class label.

378

### 379 **STATISTICAL ANALYSIS**

380

381 Statistical details for each experiment are included the figure legends. The data shown reflect the mean  
382 across these biological replicates of the mean fluorescence intensity (MFI) of approximately 2,000–3,000  
383 single, transfected cells. Error bars represent the SEM (standard error of the mean). For statistical  
384 analyses, two-tailed Student's t-tests were used to evaluate whether a significant difference exists between  
385 two groups of samples, and the reported comparisons meet the two requirements of this test: (1) the values  
386 compared are expected to be derived from a normal distribution, and (2) the variance of each group is  
387 expected to be comparable to that of the comparison group since the same transfection methodologies and  
388 data collection methods were used for all samples that were compared. A p value of  $\leq 0.05$  was considered  
389 to be statistically significant.

390

### 391 **DATA AVAILABILITY**

392

393 Data reported in composite figures (**Figs. 2a,b,d, 3a, 4b, Supplementary Fig. 4**) are included as **Source**  
394 **Data**.

395

### 396 **CODE AVAILABILITY**

397

398 Rosetta details and script are provided in **Supplementary Note 1**.

399

400 **ACKNOWLEDGEMENTS**

401  
402 This work was supported in part by the National Institute of Biomedical Imaging and Bioengineering of the  
403 NIH under Award Number 1R01EB026510 (JNL); the Northwestern University Flow Cytometry Core Facility  
404 supported by Cancer Center Support Grant (NCI 5P30CA060553); T.B.D was supported by the Department  
405 of Defense (DoD) through the National Defense Science & Engineering Graduate Fellowship (NDSEG).  
406 This work is also supported in part by the Great Lakes Bioenergy Research Center, U. S. Department of  
407 Energy, Office of Science, Office of Biological and Environmental Research under Award Number DE-  
408 SC0018409 (S.R and A.T.M). The content is solely the responsibility of the authors and does not  
409 necessarily represent the official views of the NIH, Department of Defense, Department of Energy or other  
410 federal agencies.

411  
412 **AUTHOR CONTRIBUTIONS**  
413  
414 T.B.D., A.T.M., S.R, and J.N.L conceptualized the project. T.B.D., J.D.B, W.K.C., E.E.S, created reagents,  
415 designed and performed experiments, and analyzed the data. A.N.P. assisted in analyzing and visualizing  
416 the data. A.T.M., developed the computational model and code. T.B.D., A.T.M., S.R., and J.N.L. drafted  
417 the manuscript, T.B.D., A.T.M., and A.N.P. created the figures. J.N.L. and S.R. supervised the work. All  
418 authors edited and approved the final manuscript.

419  
420 **COMPETING INTERESTS**  
421  
422 J.N.L is a co-inventor on a patent that covers the MESA technology used in this manuscript (US Patent  
423 9,732,392 B2).

424  
425



426 **REFERENCES**

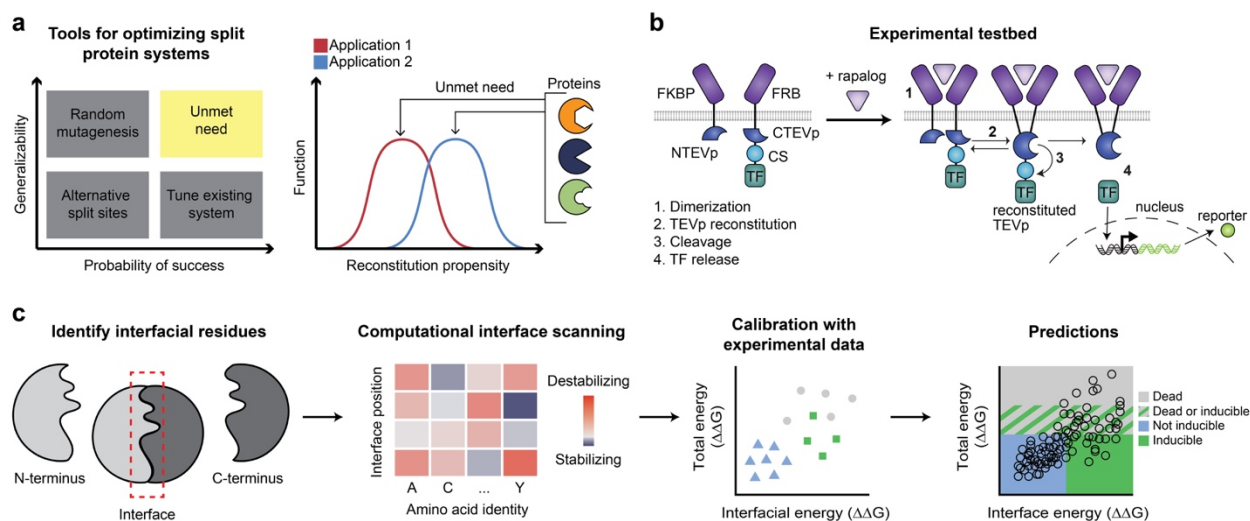
- 427 1. Romei, M.G. & Boxer, S.G. Split Green Fluorescent Proteins: Scope, Limitations, and Outlook.  
428 *Annual Review of Biophysics* **48**, 19-44 (2019).
- 429 2. Shekhawat, S.S. & Ghosh, I. Split-protein systems: beyond binary protein-protein interactions. *Curr*  
430 *Opin Chem Biol* **15**, 789-797 (2011).
- 431 3. Wehr, M.C. & Rossner, M.J. Split protein biosensor assays in molecular pharmacological studies.  
432 *Drug Discovery Today* **21**, 415-429 (2016).
- 433 4. Muller, J. & Johnsson, N. Split-ubiquitin and the split-protein sensors: chessman for the endgame.  
434 *Chembiochem* **9**, 2029-2038 (2008).
- 435 5. Paulmurugan, R. & Gambhir, S.S. Monitoring protein-protein interactions using split synthetic  
436 renilla luciferase protein-fragment-assisted complementation. *Anal Chem* **75**, 1584-1589 (2003).
- 437 6. Dixon, A.S. et al. NanoLuc Complementation Reporter Optimized for Accurate Measurement of  
438 Protein Interactions in Cells. *ACS chemical biology* **11**, 400-408 (2016).
- 439 7. Ozawa, T., Kaihara, A., Sato, M., Tachihara, K. & Umezawa, Y. Split luciferase as an optical probe  
440 for detecting protein-protein interactions in mammalian cells based on protein splicing. *Analytical*  
441 *Chemistry* **73**, 2516-2521 (2001).
- 442 8. Gray, D.C., Mahrus, S. & Wells, J.A. Activation of specific apoptotic caspases with an engineered  
443 small-molecule-activated protease. *Cell* **142**, 637-646 (2010).
- 444 9. Gao, X.J., Chong, L.S., Kim, M.S. & Elowitz, M.B. Programmable protein circuits in living cells.  
445 *Science* **361**, 1252-1258 (2018).
- 446 10. Fink, T. et al. Design of fast proteolysis-based signaling and logic circuits in mammalian cells.  
447 *Nature chemical biology* **15**, 115-122 (2019).
- 448 11. Zetsche, B., Volz, S.E. & Zhang, F. A split-Cas9 architecture for inducible genome editing and  
449 transcription modulation. *Nature biotechnology* **33**, 139-142 (2015).
- 450 12. Nihongaki, Y., Otabe, T., Ueda, Y. & Sato, M. A split CRISPR-Cpf1 platform for inducible genome  
451 editing and gene activation. *Nature chemical biology* **15**, 882-888 (2019).

- 452 13. Paulmurugan, R., Umezawa, Y. & Gambhir, S.S. Noninvasive imaging of protein-protein  
453 interactions in living subjects by using reporter protein complementation and reconstitution  
454 strategies. *Proc Natl Acad Sci U S A* **99**, 15608-15613 (2002).
- 455 14. Fetchko, M. & Stagljar, I. Application of the split-ubiquitin membrane yeast two-hybrid system to  
456 investigate membrane protein interactions. *Methods* **32**, 349-362 (2004).
- 457 15. Pandey, N., Nobles, C.L., Zechiedrich, L., Maresso, A.W. & Silberg, J.J. Combining random gene  
458 fission and rational gene fusion to discover near-infrared fluorescent protein fragments that report  
459 on protein-protein interactions. *ACS Synth Biol* **4**, 615-624 (2015).
- 460 16. Jones, K.A. et al. Development of a Split Esterase for Protein-Protein Interaction-Dependent Small-  
461 Molecule Activation. *ACS Central Science* (2019).
- 462 17. Wehr, M.C., Reinecke, L., Botvinnik, A. & Rossner, M.J. Analysis of transient phosphorylation-  
463 dependent protein-protein interactions in living mammalian cells using split-TEV. *BMC Biotechnol*  
464 **8**, 55 (2008).
- 465 18. Camacho-Soto, K., Castillo-Montoya, J., Tye, B. & Ghosh, I. Ligand-gated split-kinases. *J Am*  
466 *Chem Soc* **136**, 3995-4002 (2014).
- 467 19. Camacho-Soto, K., Castillo-Montoya, J., Tye, B., Ogunleye, L.O. & Ghosh, I. Small molecule gated  
468 split-tyrosine phosphatases and orthogonal split-tyrosine kinases. *J Am Chem Soc* **136**, 17078-  
469 17086 (2014).
- 470 20. Fink, T. et al. Design of fast proteolysis-based signaling and logic circuits in mammalian cells. *Nat*  
471 *Chem Biol* **15**, 115-122 (2019).
- 472 21. Daringer, N.M., Dudek, R.M., Schwarz, K.A. & Leonard, J.N. Modular extracellular sensor  
473 architecture for engineering mammalian cell-based devices. *ACS Synth Biol* **3**, 892-902 (2014).
- 474 22. Wehr, M.C. et al. Monitoring regulated protein-protein interactions using split TEV. *Nature Methods*  
475 **3**, 985-993 (2006).
- 476 23. Crescitelli, R. et al. Distinct RNA profiles in subpopulations of extracellular vesicles: apoptotic  
477 bodies, microvesicles and exosomes. *J Extracell Vesicles* **2** (2013).
- 478 24. Kapust, R.B., Tozser, J., Copeland, T.D. & Waugh, D.S. The P1' specificity of tobacco etch virus  
479 protease. *Biochem Biophys Res Commun* **294**, 949-955 (2002).

- 480 25. Hartfield, R.M., Schwarz, K.A., Muldoon, J.J., Bagheri, N. & Leonard, J.N. Multiplexing Engineered  
481 Receptors for Multiparametric Evaluation of Environmental Ligands. *Acs Synthetic Biology* **6**, 2042-  
482 2055 (2017).
- 483 26. Schwarz, K.A., Daringer, N.M., Dolberg, T.B. & Leonard, J.N. Rewiring human cellular input-output  
484 using modular extracellular sensors. *Nat Chem Biol* **13**, 202-209 (2017).
- 485 27. Donahue, P.S., Draut, J.W., Muldoon, J.J., Edelstein, H.I., Bagheri, N., Leonard, J.N. COMET: A  
486 toolkit for composing customizable genetic programs in mammalian cells. *bioRxiv* (2019).
- 487 28. Eisenhaber, F., Lijnzaad, P., Argos, P., Sander, C. & Scharf, M. The double cubic lattice method:  
488 Efficient approaches to numerical integration of surface area and volume and to dot surface  
489 contouring of molecular assemblies. *Journal of Computational Chemistry* **16**, 273-284 (1995).
- 490
- 491
- 492

493 **FIGURES**

494



495

496 **Fig. 1 Design-driven strategy for tuning split protein systems.** **a**, Current methods for optimizing split

497 proteins are limited (left); an ideal tool would enable adapting split proteins for multiple applications, each

498 of which may require distinct reconstitution propensities (right). **b**, This cartoon illustrates the experimental

499 testbed used here; ligand binding-induced chain dimerization results in split TEVp reconstitution, trans-

500 cleavage, and release of a previously sequestered transcription factor to drive reporter expression. **c**, Split

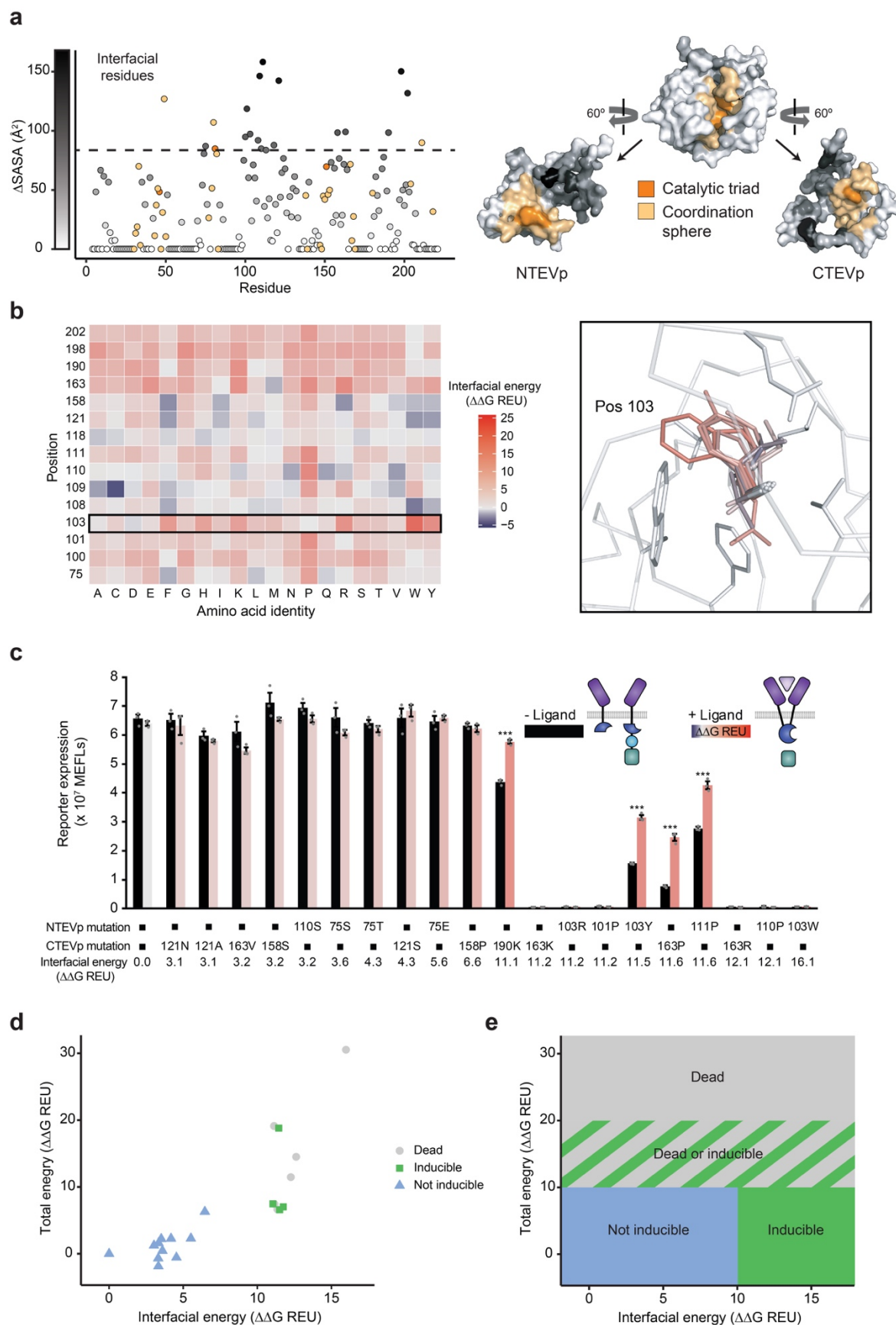
501 Protein Optimization by Reconstitution Tuning (SPORT) workflow: identify important residues at the split

502 interface which are mutable, identify mutations that alter the total and interfacial energy, and use an

503 application-specific model, trained on limited experiments, to identify those mutations that are predicted to

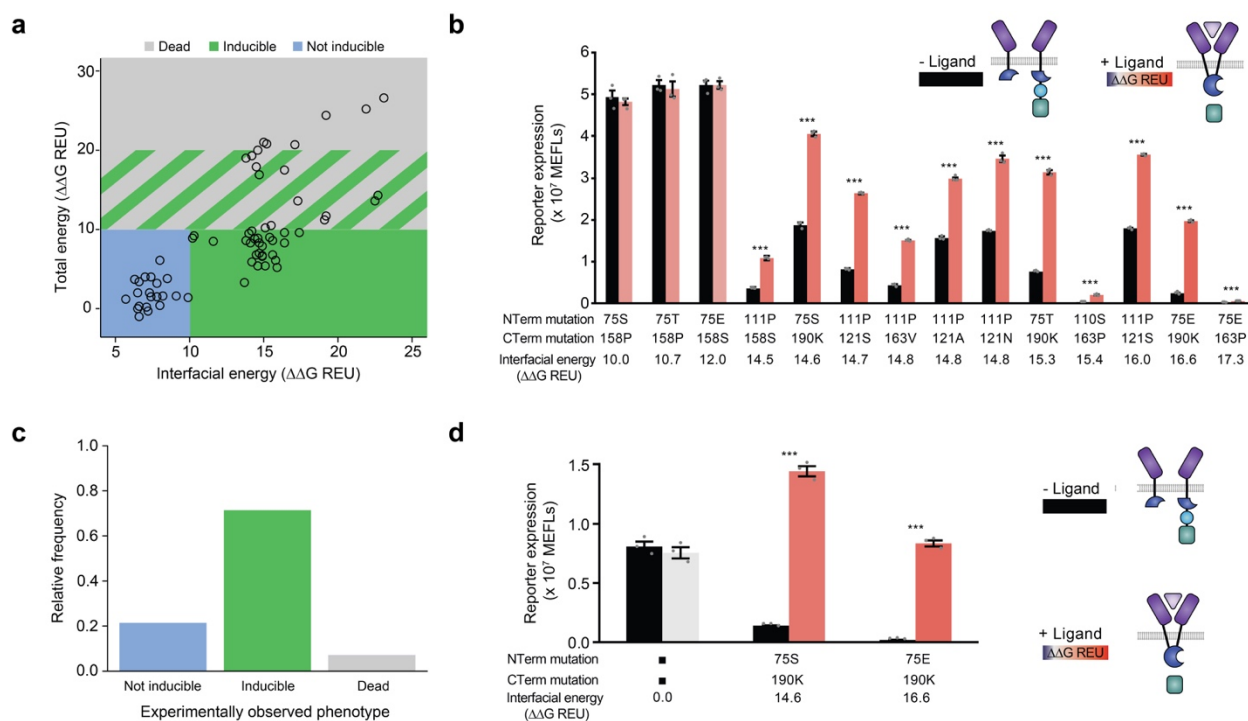
504 yield a desired functional phenotype.

505



506

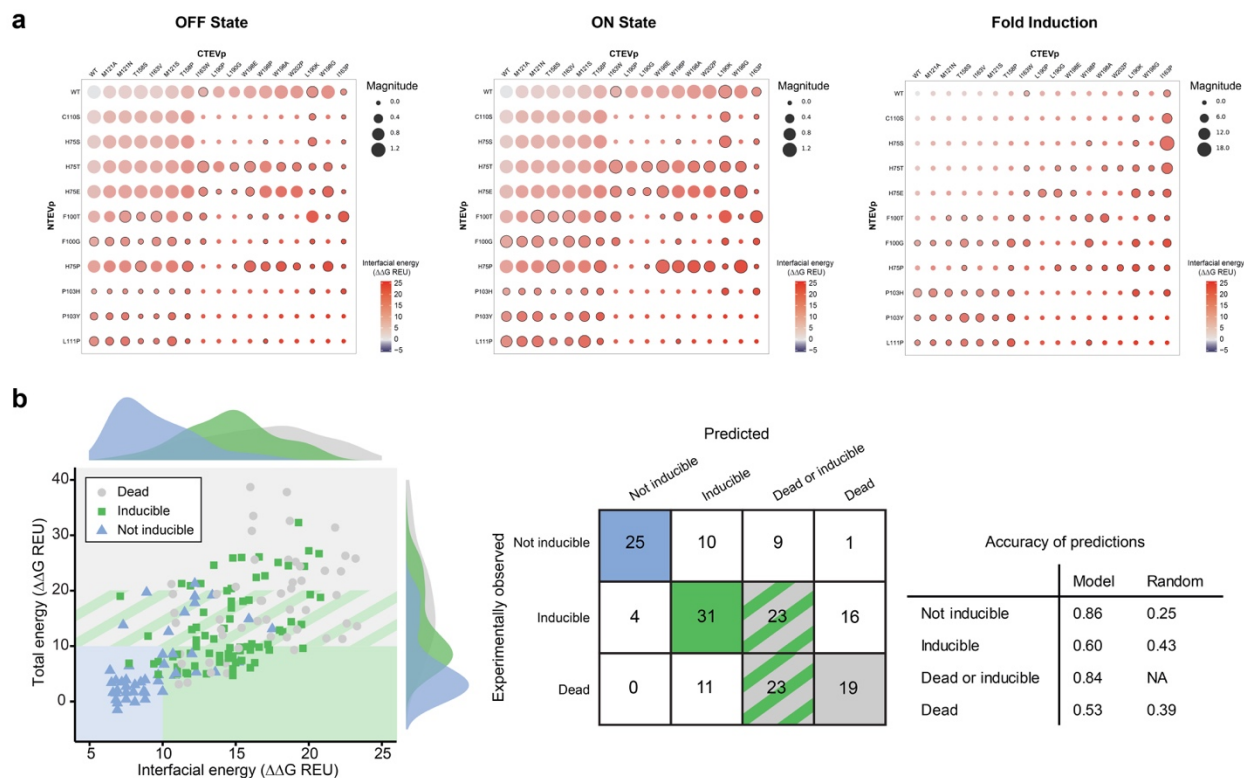
507 **Fig. 2 Computation guided method development and experimental analysis. a**, Left, characterization  
508 of the solvent accessible surface area (SASA) of each residue of 118/119 split TEVp. Right, 3D depiction  
509 of 118/119 split TEVp, showing the catalytic triad (orange), coordination sphere (yellow), and  $\Delta$ SASA  
510 (greyscale). **b**, Mutational scanning of high  $\Delta$ SASA residues (left) and example of all possible mutations of  
511 residue 103 (right), with change in interfacial energy indicated by color. **c**, Experimental analysis of TEVp  
512 mutations predicted to span a range of interfacial energies. Error bars depict S.E.M. (\* $p \leq 0.05$ , \*\*\* $p \leq$   
513  $0.001$ ). **d**, Experimental phenotypes observed in **c** were plotted on an energy landscape and annotated as  
514 indicated by color (reporter expression normalized to WT  $< 0.05$  is “dead”, fold induction  $< 1.2$  is “not  
515 inducible”, fold induction  $\geq 1.2$  is “inducible”). **e**, Proposed model for predicting zones of functional  
516 phenotypes based upon total and interfacial energy; the boundaries were proposed based upon  
517 observations using the initial 20 mutants tested in **c**.  
518



519

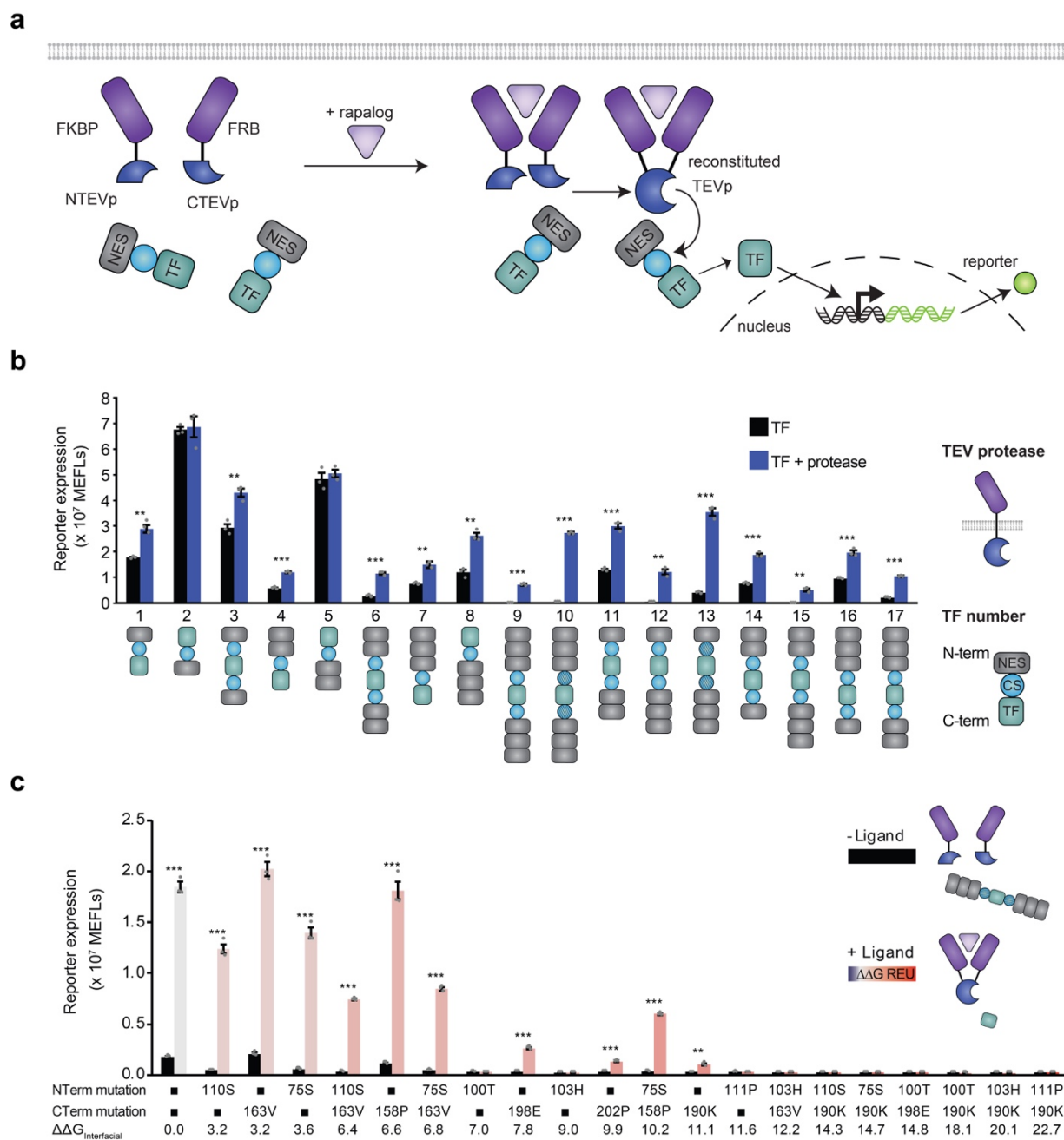
520 **Fig. 3 Evaluation of model-predicted phenotypes for combined mutations.** **a**, Computed energies and  
 521 predicted phenotypes based on the classifier model—proposed in **Fig. 2e**—of all possible double and  
 522 paired mutants constructed by combinatorial sampling of the initial single mutants tested (omitting dead  
 523 mutations) in **Fig. 2c**. **b**, Experimental evaluation of selected mutants predicted to be inducible. **c**,  
 524 Experimentally observed phenotypes for the fourteen mutants predicted to be inducible (from **b**), showing  
 525 that the model predicts inducibility at a fairly high rate (10/14). **d**, Normalizing protein expression levels  
 526 improves performance (fold induction) of selected mutants (from **b**), whereas WT function is not changed.  
 527 Normalization was achieved using Western Blot analysis (**Supplementary Fig. L4**) to adjust DNA doses  
 528 transfected (per well, N-terminal chains: 0.4 ng WT, 1 ng 75S, 1.4 ng 75E; C-terminal chains: 5 ng WT, 12  
 529 ng 190K). Error bars depict S.E.M. (\* $p \leq 0.05$ , \*\*\* $p \leq 0.001$ ).

530



531  
 532 **Fig. 4 Evaluation of model-predicted phenotypes for novel mutations and combinations.** **a**, For each  
 533 experimentally characterized construct, reporter output was quantified in the absence of ligand (OFF state)  
 534 and following ligand addition (ON state), and the fold induction was calculated. Calculated interfacial energy  
 535 for each construct is indicated by circle *color*, magnitude of reporter expression (or fold-induction) is  
 536 indicated by circle *size*, and constructs with a fold induction  $\geq 1.2$  are denoted with a black border. Single  
 537 mutants observed to be dead (**Fig. 2**) were not carried forward to this analysis. **b**, Left, experimentally  
 538 observed phenotypes (data point color) were mapped onto the proposed classifier model from **Fig. 2e**, with  
 539 observed frequency distributions shown as histograms. Right, evaluation of model prediction accuracy  
 540 compared to random assignment of phenotypes.  
 541



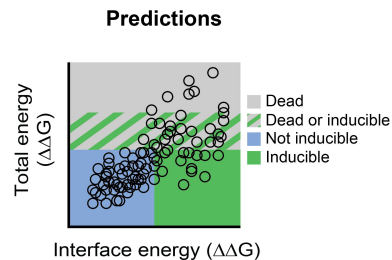
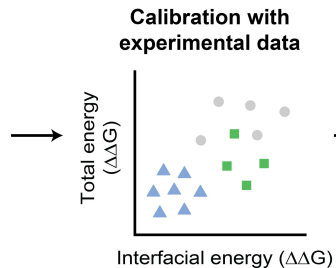
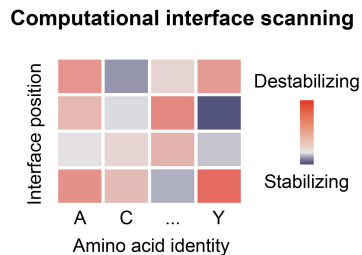
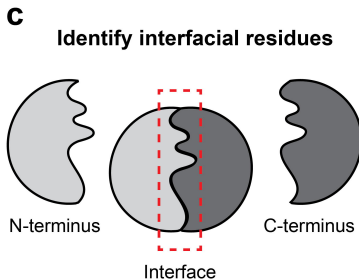
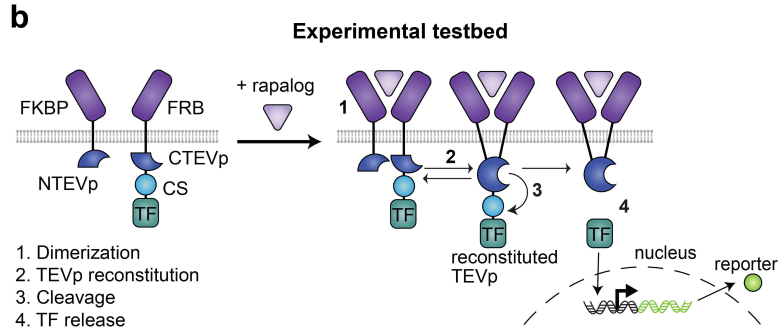
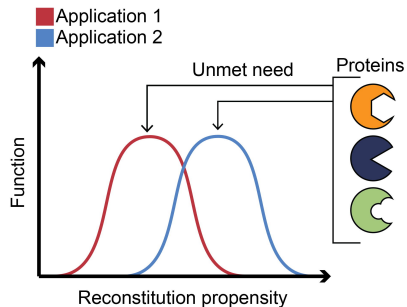
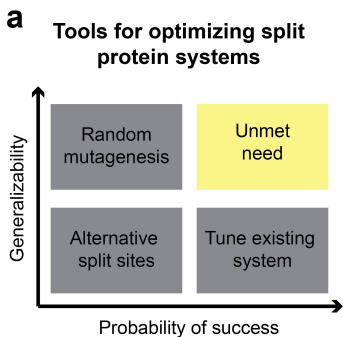


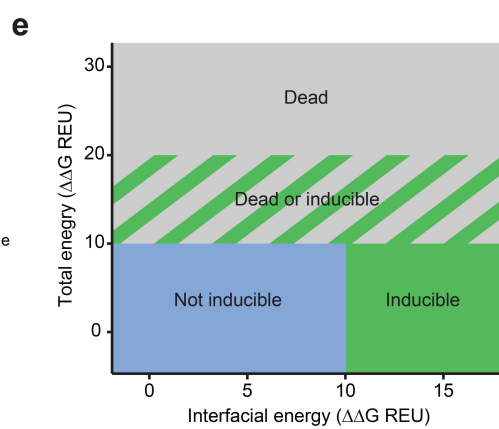
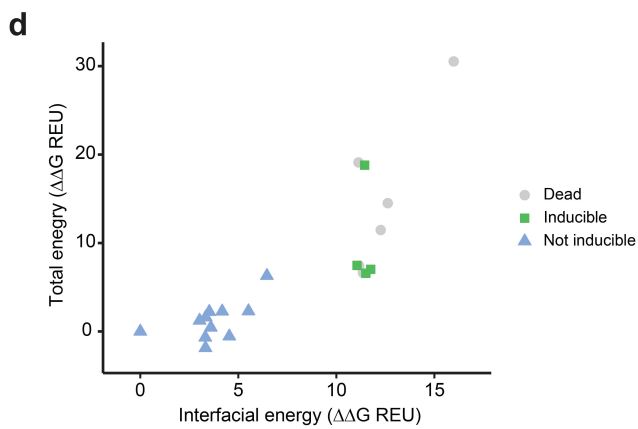
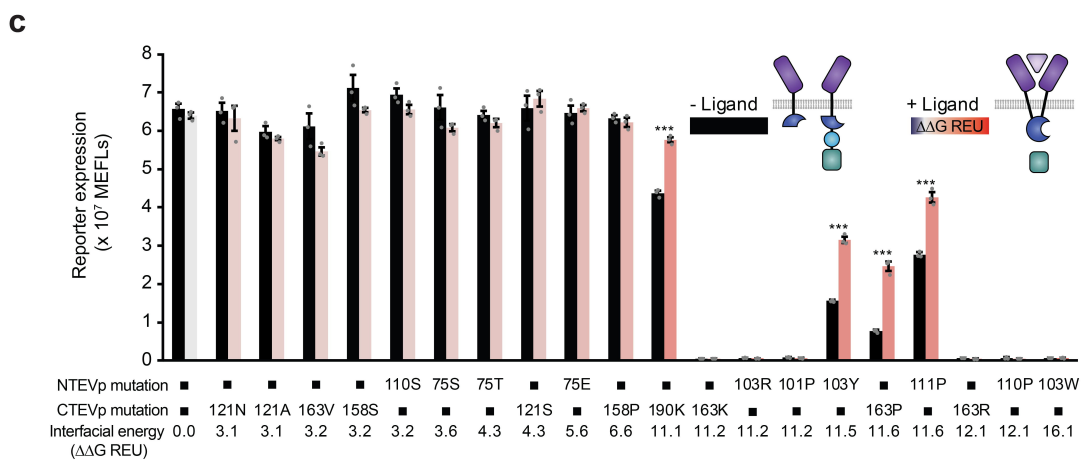
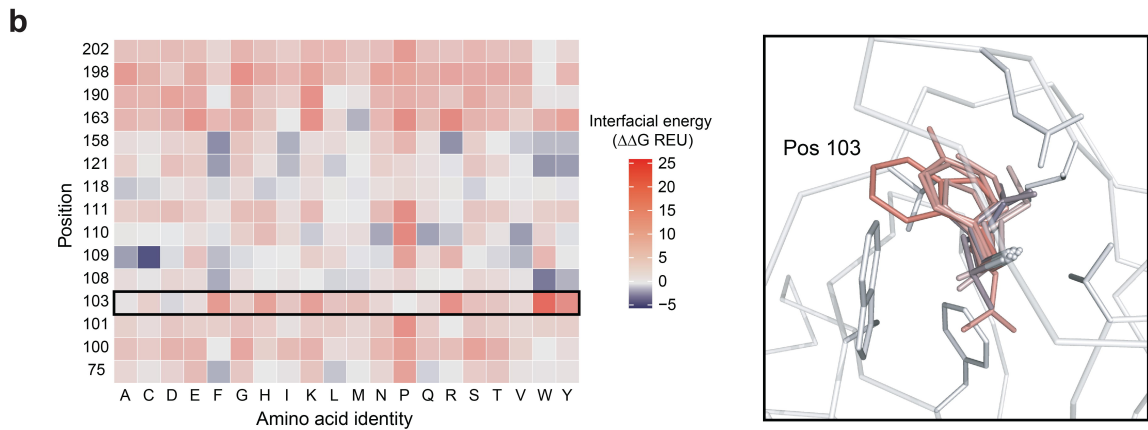
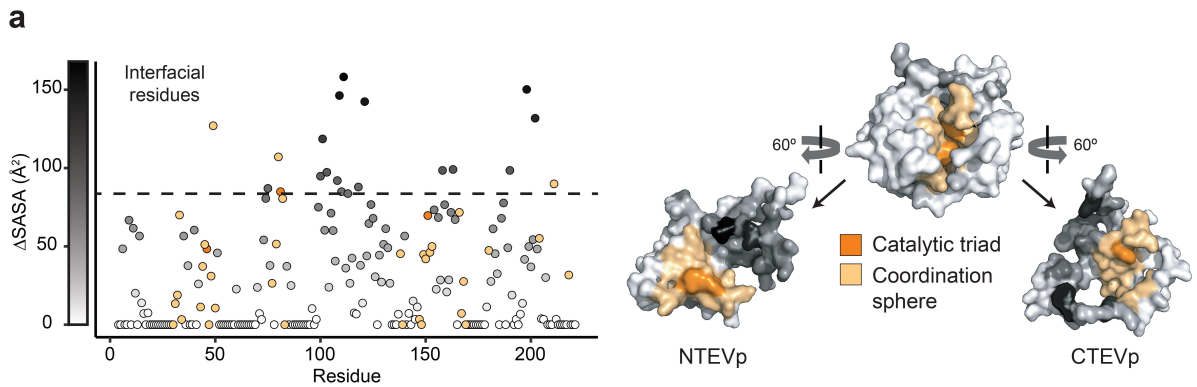
542

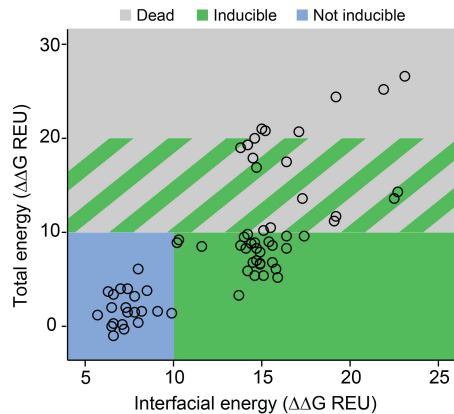
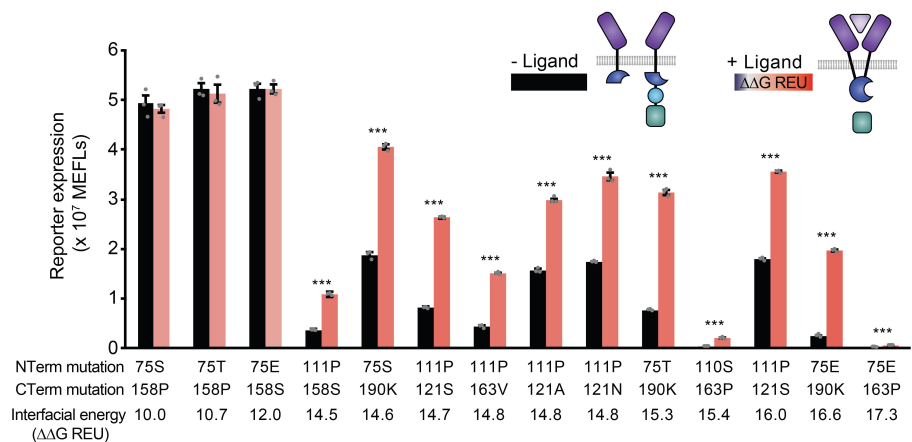
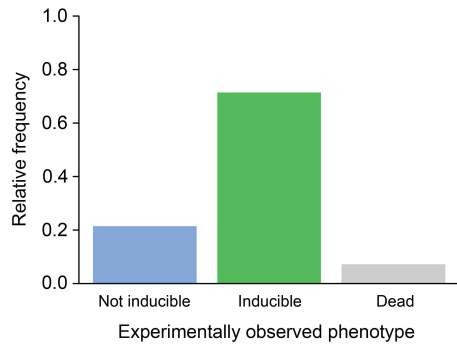
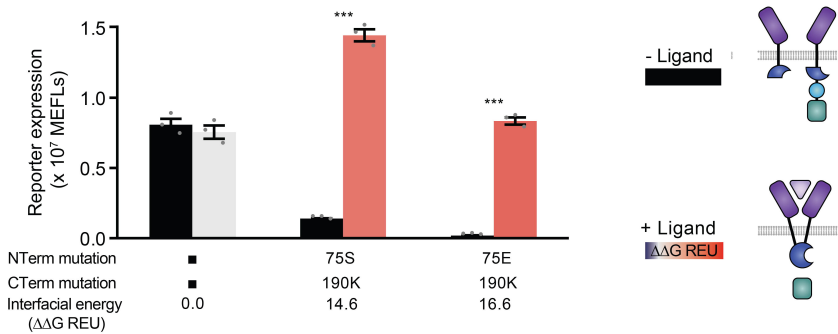
543 **Fig. 5 Model guided design of a new split TEVp application in soluble context.** **a**, This cartoon  
 544 illustrates the soluble split TEVp testbed. Ligand-binding-induced dimerization mediates reconstitution of  
 545 split TEVp, which then cleaves one or more nuclear export sequence (NES) elements from a soluble  
 546 transcription factor, leading to nuclear import and reporter expression. **b**, Developing the testbed by  
 547 evaluating engineered transcription factors (TF) for consistency with the mechanism proposed in **a**; shaded  
 548 cleavage sequence (CS) domains indicate a G residue in the P1' position, unshaded CS domains indicate

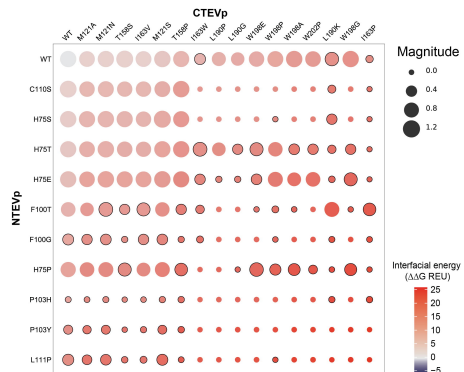
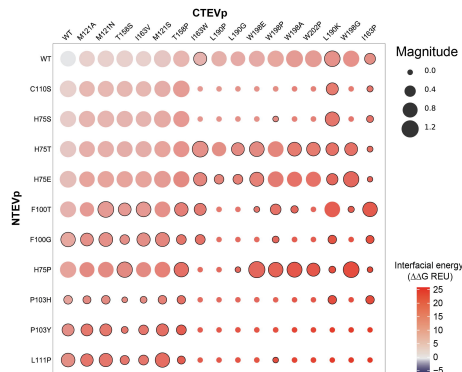
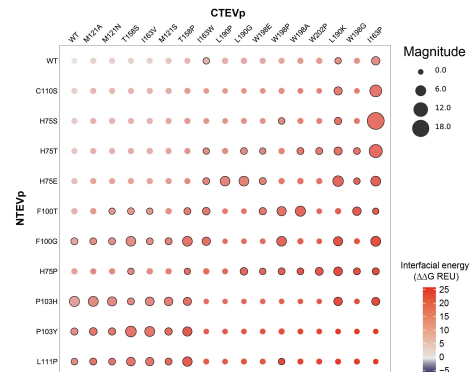
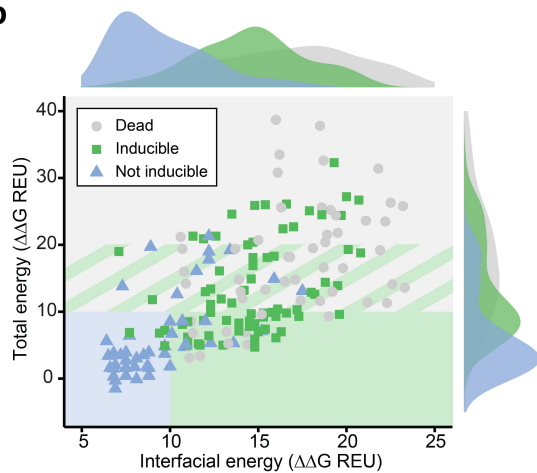
549 a M residue in this position.<sup>24</sup> **c**, Experimental analysis of single and paired mutants sampling a range of  
550 interfacial energies (indicated by color and labeled), employing TF10 from **b**. Error bars depict S.E.M. (\* $p \leq$   
551 0.05, \*\*\* $p \leq 0.001$ ).

552





**a****b****c****d**

**a****OFF State****ON State****Fold Induction****b**

		Predicted			
		Not inducible	Inducible	Dead or inducible	Dead
Experimentally observed	Not inducible	25	10	9	1
	Inducible	4	31	23	16
	Dead	0	11	23	19

Accuracy of predictions

	Model	Random
Not inducible	0.86	0.25
Inducible	0.60	0.43
Dead or inducible	0.84	NA
Dead	0.53	0.39

